Infrared Spatial and Frequency Selective Metamaterial with Near-Unity Absorbance

Xianliang Liu,[1] Tatiana Starr,[2] Anthony F. Starr,[2] and Willie J. Padilla[1,*]

[1]*Department of Physics, Boston College, 140 Commonwealth Avenue, Chestnut Hill, Massachusetts 02467, USA*
[2]*SensorMetrix, Inc., San Diego, California 92121, USA*

We demonstrate, for the first time, a spatially dependent metamaterial perfect absorber operating in the infrared regime. We achieve an experimental absorption of 97% at a wavelength of 6.0 μm, and our results agree well with numerical full-wave simulations. By using two different metamaterial sublattices we experimentally demonstrate a spatial and frequency varying absorption which may have many relevant applications, including hyperspectral subsampling imaging.

Since the first experimental demonstration of negative refractive index [1–4], research into metamaterials has grown enormously. The ability of metamaterial to achieve nearly any electromagnetic response in nearly any frequency band suggests many exotic applications including invisibility cloaks [5] and perfect lenses [6,7]. One current expanding field of research is that of metamaterial perfect absorbers (MPAs) due to their unique ability to achieve unity absorption with high efficiency [8]. Here we present a computational and experimental study of an infrared metamaterial absorber which realizes 97% absorption at 6.0 μm wavelength. By using two different metamaterial sublattices consisting of a MPA and a near zero absorber, we experimentally demonstrate a spatial and frequency varying absorption which may have many relevant applications.

Metamaterials, through changes of the size and shape of subwavelength metallic elements, permit the amplitude and frequency tuning of both the electric [$\epsilon(\omega)$] and magnetic [$\mu(\omega)$] response of electromagnetic radiation. Although this electromagnetic response is resonant and narrow band, there have been demonstrations of exotic metamaterials operating in all relevant bands for frequencies below visible [9–14]. The resonant nature of metamaterials results in a strong focusing of the electric field within gaps of the structure, thus providing a means to dynamically control the resonance frequency, phase, and amplitude [15–17]. By using either passive or active external stimuli, temperature, electric field, optical, etc., dynamical MPAs may be explored and extended to much of the electromagnetic spectrum [18,19]. After first demonstration of the microwave MPA, many efforts have focused on extending highly absorbing metamaterials to smaller wavelengths. To date, most studies have been carried out in the terahertz regime and absorptions as high as 96.8% have been achieved [18].

Currently, there is great interest in single-pixel imaging, based on the theory of compressive sensing [20–22]. Typically, experimental realization of these systems utilizes spatial light modulators (SLMs) for encoding random spatial patterns in the wave front of transmitted or reflected optical radiation [23,24]. In the THz frequency regime metamaterials have shown promise to be used as SLMs in a transmission configuration [25]. At visible wavelengths single-pixel imagers may use liquid crystals or microelectromechanical systems to manipulate the spatial profile of the beam. However, at lower infrared frequencies liquid crystals are inefficient, thus preventing their use. Further, for many applications, mechanical manipulation of the incoming image may not be feasible. An intriguing application of metamaterial absorbers would be their use as a SLM in a subsampling infrared imaging system. However, to date, metamaterial absorbers have only been demonstrated in the microwave and THz frequency regimes.

The schematic of a single unit cell of an infrared MPA is shown in Figs. 1(a) and 1(b), and consists of two metallic elements: a cross-shaped resonator and ground plane. We space these metallic elements apart by virtue of a dielectric layer. The cross resonator is a type of electric ring resonator (ERR) [5,26] and couples strongly to uniform electric fields, and negligibly to magnetic fields. However, by paring the ERR with a metallic ground plane, the magnetic component of light couples to both the center section of the cross resonator and the ground plane, thus generating antiparallel currents resulting in resonant response. The magnetic response can therefore be tuned independent of the electric, by changing the geometry of the ERR and the distance between elements. By tuning the amplitude and frequency location of the electric and magnetic resonances it is possible to match the impedance $Z(\omega) = \sqrt{\mu(\omega)/\epsilon(\omega)}$ of the MPA to free space, thus minimizing the reflectance at a specific frequency. The metallic ground plane is thicker than the penetration depth of light in the IR range and thus transmission of the MPA is zero. These two conditions thus lead to narrow band high absorption.

The optimized structure presented in Fig. 1 was obtained through computer simulations using the commercial program CST Microwave Studio 2009. The time domain solver was utilized and metallic portions of the metamate-
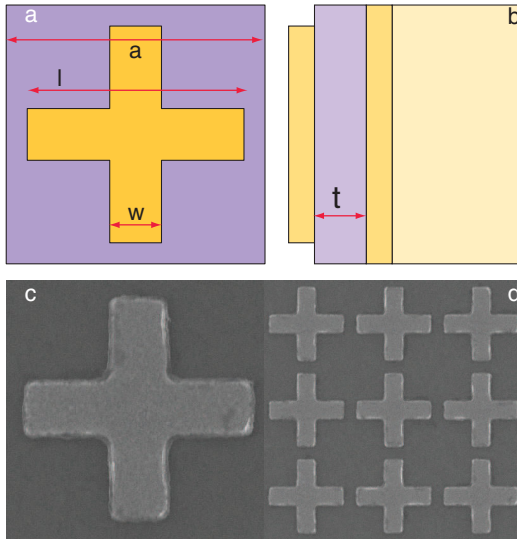
FIG. 1 (color online). Design and fabrication of the infrared metamaterial absorber. (a) Schematic of a MPA unit cell and its optimized dimensions are $a = 2$, $l = 1.7$, $w = 0.4$, $t = 0.185$ in micrometers. (b) Side view of the unit cell. (c) Scanning electron microscope (SEM) image of one unit cell. (d) SEM image of a periodically patterned array.

rial absorber were modeled as gold using a Drude model with a plasma frequency $\omega_p = 2\pi \times 2175$ THz and collision frequency $\omega_c = 2\pi \times 6.5$ THz [27]. We use Al_2O_3 as the dielectric spacer and simulate the dielectric constant and loss tangent as 2.28 and 0.04, respectively. The transmission $T(\omega) = |S_{21}(\omega)|^2$ and reflection $R(\omega) = |S_{11}(\omega)|^2$ were obtained from S-parameter simulations with appropriate boundary conditions to approximate a TEM wave incident on the structure with both electric and magnetic field vectors lying in plane and the wave vector perpendicular. The frequency dependent absorption was calculated as $A(\omega) = 1 - R(\omega) - T(\omega)$ where, as expected for the present design, S_{21} is nearly zero across the entire frequency range due to the metallic ground plane. The optimized structure, Fig. 1(a), achieves a simulated maximum absorption at 6.0 μm and has the geometrical parameters (in microns) of $a = 2.0$, $l = 1.7$, $w = 0.4$, $t = 0.185$, and the thickness of both metallizations was 0.1 μm. The simulated $R(\omega)$, $T(\omega)$, and $A(\omega)$ are shown in Fig. 2(a).

Simulations indicate the feasibility of realizing an infrared MPA, and we now thus turn toward experimental demonstration. Fabrication begins with E-beam deposition of a 100 nm thick layer of gold on a silicon substrate. This is followed by atomic layer deposition of a 185 nm thick layer of Al_2O_3. Resist 950 PMMA-A (MicroChem) was then spin coated on top and patterned using E-beam lithography. Another 100 nm thick layer of gold was E-beam evaporated followed by liftoff in acetone. Figure 1(c) displays a scanning electron microscope (SEM) image of a single unit cell of the fabricated sample, and Fig. 1(d)
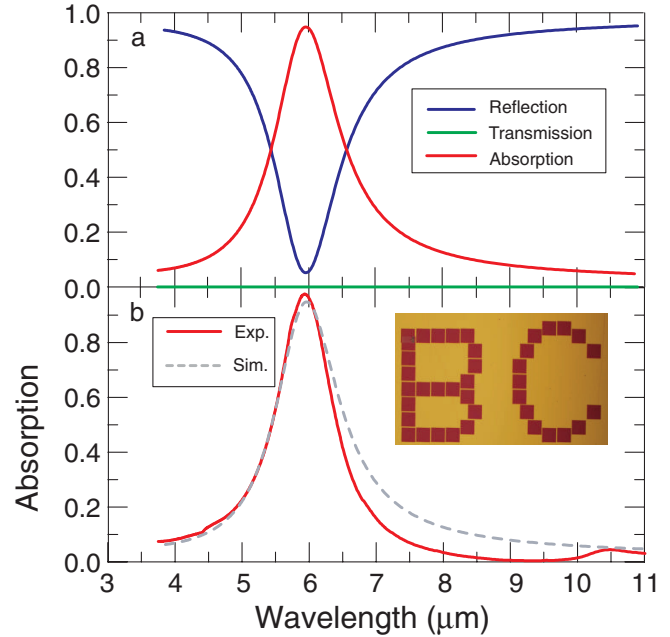

FIG. 2 (color online). Simulated and experimental performance of the infrared metamaterial absorber. (a) Numerical simulations of the electromagnetic response: Reflection (blue line), transmission (green line), and absorption (red line). The maximum absorption at 6 μm is 97%. (b) A comparison between the experimental absorption (red line) and simulated absorption (dashed gray line). Inset of (b) shows an optical microscope image of the fabricated spatially dependent metamaterial absorber.

shows a larger field of view. The total lateral size of the sample was 140 μm $\times$ 140 μm.

Transmission and reflection were characterized from a wavelength of 3–12 μm using a Fourier-transform infrared spectrometer combined with an infrared microscope (liquid-N_2-cooled MCT detector, 15$\times$ cassegrain objective lens and KBr beam splitter). The reflection was measured at an incident angle of 20° and transmission was measured at normal incidence. The measured reflection spectra are normalized with respect to a gold mirror while the transmission spectrum is normalized with respect to an open aperture. The measured transmission and reflection are then used to calculate the absorption.

The experimental absorption is shown in Fig. 2(b) as the solid red curve. As shown in Fig. 2(a) the simulated transmission is effectively 0 across the entire range and a resonance occurs in the simulated reflectance at 6 μm where $R = 0.03$, thus yielding a maximum in the simulated absorption. The experimental absorption has a maximum at 6.0 μm with a value of 97%, with relatively low values to both lower and higher frequencies. The absorption has a full width half maximum of 1.0 μm and, at wavelengths of 4 and 10 μm $A(\omega)$, has fallen off to 10% and 1%, respectively. We achieve good agreement between experimental and simulated (dashed gray curve) absorptivities, as is evident from Fig. 2(b).
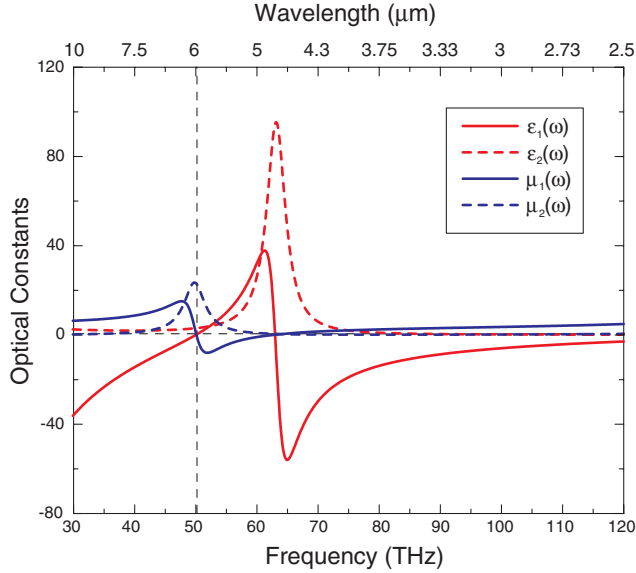
FIG. 3 (color online).   Extracted optical constants for the simulated design.

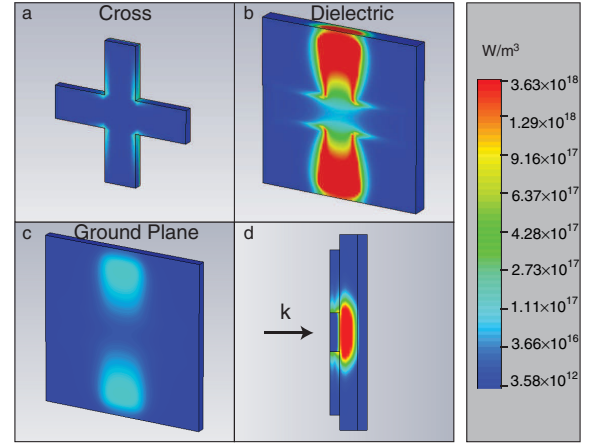

FIG. 4 (color online).   Energy dissipation in the MPA structure at a wavelength of 6 μm. Energy dissipation distribution in (a) cross, (b) dielectric spacer, (c) ground plane, and (d) top view of the whole structure.

The optical constants were extracted for the present MPA design via inversion of the S parameters [28]. The retrieved $[\epsilon(\omega)]$ and $[\mu(\omega)]$ are displayed in Fig. 3, where the vertical dashed line indicates the frequency (ω_0) of the absorption maximum (A_m). As can be observed, the real parts of the optical constants both cross zero at ω_0—as required for zero reflection. Note also that either $\epsilon_1(\omega)$ or $\mu_1(\omega)$ is always negative, i.e., when $\epsilon_1(\omega) > 0$, $\mu_1(\omega)$ goes negative and vice versa. This is required for zero transmission across this range. By using the optical constants displayed in Fig. 3 we are able to recalculate $R(\omega)$, $T(\omega)$, and $A(\omega)$, not shown, thus verifying their validity. To further investigate the underlying absorption mechanism and to understand its various contributions, we computationally monitor energy dissipation in the MPA multilayer structure. The simulated energy loss is shown in Fig. 4 for each layer of the MPA [4(a)–4(c)] and for the structure as a whole [4(d)]. Simulations reveal that the majority of energy is dissipated as dielectric loss within the Al_2O_3 layer and is an order of magnitude greater than the Ohmic loss within the metallic cross and ground plane.

In order to demonstrate the versatility of the MPA and its potential for applications, we combined our highly absorbing metamaterial, which we now term unit cell A (UCA), with an extremely low absorbing metamaterial, unit cell B (UCB). This is a type of metamaterial consisting of different sublattices, of which both bipartite [29] and tripartite [30] variations have been demonstrated. Unit cell B is of identical lateral proportions as UCA, i.e., 2 μm × 2 μm, and consists of the same metallic ground plane and Al_2O_3 dielectric with identical thicknesses. We use each of these two unit cells to form a pattern in the xy plane; i.e., we form a spatially selective or ''graded'' perfect absorber. The inset of Fig. 2(b) displays an optical microscope image of just such a design, forming the two letters ''B'' and ''C.'' The pattern of UCA consisted of 39 writing fields, each of dimensions 140 μm × 140 μm, where each contains nearly 5000 metamaterial unit cells. To avoid overlap we use a 4 μm space between neighboring UCA writing fields.

We characterized the graded metamaterial absorber using the same experimental setup as described earlier. A computer controlled linear stage moved automatically in the xy plane and we collected both R and T from wavelengths of 20 μm–600 nm. Reflection spectra is normalized with respect to a Au mirror with the same beam size. A spatial resolution of 50 μm was used, thus creating an image with 40 pixels along the x axis and 28 along the y axis. A total of 16 000 interferogram points were collected for each pixel. A two-dimensional hyperspectral image is acquired, with a total data cube size of 1.8×10^7, thus permitting investigation of both the frequency and spatial dependence of the sample.

We display 3D images of the data for a wavelength of 6 μm, shown in Figs. 5(a) and 5(b). The image is displayed as (x, y, A) and thus the $\hat{x}$ and $\hat{y}$ axes indicate the dimensions of the pattern and the $\hat{z}$ axis displays the absorption for each pixel. Clearly, as demonstrated in Fig. 5(a), at the resonance frequency of $\lambda = 6$ μm, the patterned metamaterial (unit cell A) achieves near-unity absorption. Figure 5(b) shows the x-z plane from which it can be directly observed that absorption is near zero for UCB. Thus by using bipartite unit cells with perfect absorption and with near zero absorption, we have maximized contrast of the image.

In order to show the frequency dependence of the spatially selective MPA, in Figs. 5(c) and 5(d) we plot 3D images for a wavelength of $\lambda = 10$ μm. Data are in the form (x, y, R), where R is the reflectance, for Fig. 5(c) and (x, y, A) for Fig. 5(d). As can be observed, the reflectance is
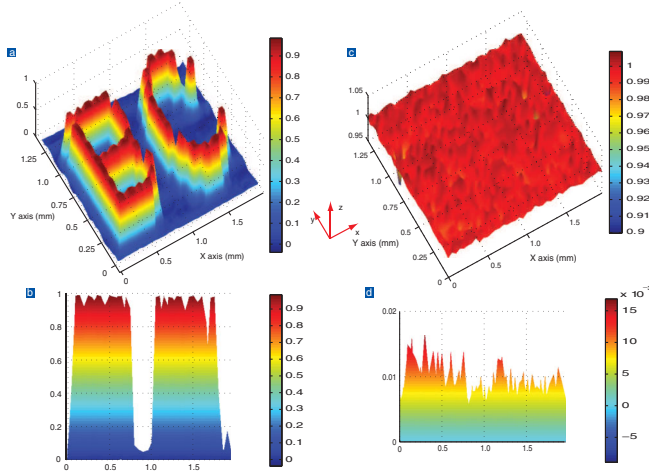
FIG. 5 (color online).   Experimental three-dimensional images of the absorption and reflection of the graded metamaterial absorber. (a) Spatially dependent absorption image at a wavelength of 6 μm (plotted to 100% absorption). (b) x-z view of the absorption at 6 μm. (c) Image of the reflection at a wavelength of 10 μm. (d) x-z view of the reflection at 10 μm.

close to unity over the xy plane and, correspondingly, the absorption is near zero. A perfect metal at these wavelengths would give 100% reflectance and zero absorption. In contrast to both the optical photograph [Fig. 2(b)], and the image at 6 μm [Fig. 5(a)], at $\lambda = 10$ μm the MPA is not visible, i.e., indistinguishable from a perfect metal.

In conclusion, we have designed, fabricated, and characterized a midinfrared metamaterial perfect absorber, which achieves an experimental absorption of 97% at a wavelength of 6.0 μm. We further patterned the MPA to demonstrate the ability of achieving both a frequency and spatially selective absorption. Since one may specify a particular spatial pattern to be sent to a detector and the other component to be strongly absorbed, we have the ability to spatially modulate signals with large dynamic range. Dynamical range as large as 40 dB is achieved for our MPA without optimization, which is comparable to existing digital cameras [31]. These results suggest an alternative way to achieve spatial light modulation, information coding, and single-pixel imaging. Interestingly, by combining the MPA with dynamical control [15,16], the option of performing real-time subsample imaging, and hyperspectral subsample imaging, becomes possible. One advantage of dynamical metamaterials is that they may be fabricated with no moving parts [16]; i.e., they are all solid

state. Because of the scalability of metamaterials, the concept of a spatially selective MPA suggests the ability of constructing SLMs which may operate at any subvisible frequency. The above listed advantages possible with metamaterials suggest exotic applications—in particular, hyperspectral single-pixel imaging cameras, which may alleviate the typically incurred trade-offs between cost, speed, signal-to-noise ratio, spectral resolution, and spatial resolution.

*willie.padilla@bc.edu
[1] V. G. Veselago, Sov. Phys. Usp. **10**, 509 (1968).
[2] D. R. Smith *et al.*, Science **305**, 788 (2004).
[3] D. R. Smith *et al.*, Phys. Rev. Lett. **84**, 4184 (2000).
[4] R. A. Shelby *et al.*, Science **292**, 77 (2001).
[5] D. Schurig *et al.*, Science **314**, 977 (2006).
[6] J. B. Pendry, Phys. Rev. Lett. **85**, 3966 (2000).
[7] N. Fang *et al.*, Science **308**, 534 (2005).
[8] N. I. Landy *et al.*, Phys. Rev. Lett. **100**, 207402 (2008).
[9] V. M. Shalaev *et al.*, Opt. Lett. **30**, 3356 (2005).
[10] S. Linden *et al.*, Science **306**, 1351 (2004).
[11] S. Zhang *et al.*, Phys. Rev. Lett. **94**, 037402 (2005).
[12] T. J. Yen *et al.*, Science **303**, 1494 (2004).
[13] M. Bayindir *et al.*, Appl. Phys. Lett. **81**, 120 (2002).
[14] M. C. K. Wiltshire *et al.*, Science **291**, 849 (2001).
[15] H.-T. Chen *et al.*, Nat. Photon. **2**, 295 (2008).
[16] H.-T. Chen *et al.*, Nature (London) **444**, 597 (2006).
[17] H.-T. Chen *et al.*, Nat. Photon. **3**, 148 (2009).
[18] H. Tao *et al.*, Phys. Rev. B **78**, 241103(R) (2008).
[19] H. Tao *et al.*, Opt. Express **16**, 7181 (2008).
[20] D. L. Donoho, IEEE Trans. Inf. Theory **52**, 1289 (2006).
[21] E. J. Candes *et al.*, IEEE Trans. Inf. Theory **52**, 5406 (2006).
[22] E. J. Candes, in *Proceedings of the International Congress of Mathematicians, Madrid, 2006* (European Mathematical Society, Madrid, 2006), Vol. 3, p. 1433.
[23] M. E. Gehm *et al.*, Opt. Express **15**, 14013 (2007).
[24] W. L. Chan *et al.*, Appl. Phys. Lett. **93**, 121105 (2008).
[25] W. L. Chan *et al.*, Appl. Phys. Lett. **94**, 213511 (2009).
[26] W. J. Padilla *et al.*, Phys. Rev. B **75**, 041102(R) (2007).
[27] M. A. Ordal *et al.*, Appl. Opt. **22**, 1099 (1983).
[28] D. R. Smith *et al.*, Phys. Rev. B **65**, 195104 (2002).
[29] Y. Yuan *et al.*, Opt. Express **16**, 9746 (2008).
[30] C. M. Bingham *et al.*, Opt. Express **16**, 18 565 (2008).
[31] S. Battiato *et al.*, J. Electron. Imaging **12**, 459 (2003).